

SHED Light on Segmentation for Dense Prediction

Seung Hyun Lee¹ Sangwoo Mo² Stella X. Yu¹

Abstract

Dense prediction infers per-pixel values from a single image and is fundamental to 3D perception and robotics. Although real-world scenes exhibit strong structure, existing methods treat it as an independent pixel-wise prediction, often resulting in structural inconsistencies. We propose SHED, a novel encoder-decoder architecture that enforces geometric prior explicitly by incorporating segmentation into dense prediction. By bidirectional hierarchical reasoning, segment tokens are hierarchically pooled in the encoder and unpooled in the decoder to reverse the hierarchy. The model is supervised only at the final output, allowing the segment hierarchy to emerge without explicit segmentation supervision. SHED improves depth boundary sharpness and segment coherence, while demonstrating strong cross-domain generalization from synthetic to the real-world environments. Its hierarchy-aware decoder better captures global 3D scene layouts, leading to improved semantic segmentation performance. Moreover, SHED enhances 3D reconstruction quality and reveals interpretable part-level structures that are often missed by conventional pixel-wise methods.

1. Introduction

Dense prediction tasks, such as monocular depth estimation and semantic segmentation, serve as the foundation for spatial reasoning in robotics (Liu et al., 2024). At their core, these tasks require an understanding of how 2D image projections relate to the underlying 3D structure of the world. However, modern state-of-the-art models based on Vision Transformers (ViTs) (Dosovitskiy, 2020) and pixel-wise regression often treat these tasks as a collection of independent point estimations rather than a coherent structural reconstruction. This disconnect frequently results in structural leakage, where predicted boundaries do not align with

¹University of Michigan ²POSTECH. Correspondence to: Stella X. Yu <stellayu@umich.edu>.

physical objects, leading to blurred edges and inconsistent surface geometry (Figure 1, row 1).

In contrast, the human visual system does not process images as an array of independent points. Instead, it employs a sophisticated bidirectional hierarchy (Hochstein & Ahissar, 2002). Our perception integrates depth and segmentation through a feedback loop where a global scene layout is first inferred by grouping fine-grained textures into parts and wholes. This high-level structural scaffold then guides the refinement of local details. This part-whole reasoning ensures that local pixel-level predictions are constrained by the global geometric context. This organization results in depth maps characterized by sharp, high-fidelity boundaries and smooth intra-object variations (Figure 1, row 2).

To realize this idea, we propose **SHED**, Segment Hierarchy for Dense Prediction, a novel architecture that re-conceptualizes dense prediction as a process of hierarchical structural reasoning. Unlike traditional models that decode latent features directly back to a rigid pixel grid, SHED learns an implicit hierarchy of segments that adaptively decompose the scene. Note that these segments are not provided via external supervision. They are learned end-to-end, guided solely by the dense prediction objective.

The technical core of SHED lies in its symmetric bidirectional flow. While the encoder iteratively groups pixels into increasingly abstract segment tokens, our contribution focuses on the structural inversion of this process in the decoder. To produce a structured dense map, SHED’s decoder unpools features from coarser segments to finer ones using probabilistic assignments computed during the encoding phase. This reverse hierarchy, which has no counterpart in encoder-only segmentation frameworks, enables coarse structural context to directly constrain fine-grained predictions. By distributing segment-level features across associated regions, the model naturally enforces sharp boundaries between distinct objects and maintains geometric smoothness within a single surface. This mechanism allows high-level geometric priors to strictly inform the pixel-level output, preserving the global layout while capturing fine-grained structural detail.

Integrating hierarchical segmentation into the dense prediction pipeline grants SHED three key advantages:

- SHED produces depth maps with high-fidelity bound-

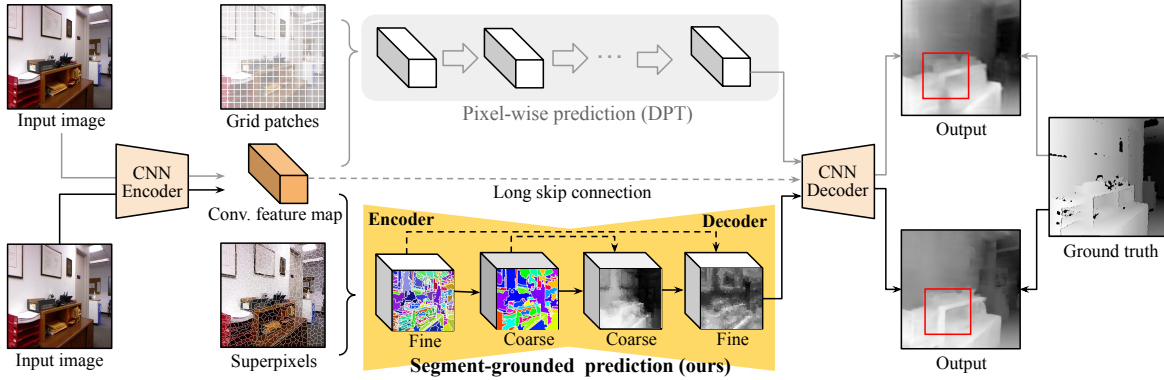


Figure 1. Segment hierarchy for dense prediction (SHED). Conventional methods such as DPT (Ranftl et al., 2021) perform pixel-wise prediction without considering structure, often resulting in blurry object shapes. SHED addresses this by leveraging a hierarchy of segment tokens to guide prediction. Unlike DPT, which uses fixed grid tokens across all layers, we adapt its ViT (Dosovitskiy, 2020) blocks into two stages: the encoder pools superpixel tokens into coarser segment tokens, and the decoder progressively refines predictions from coarse to fine segments, producing depth maps with structural coherence.

ary alignment. This inherent structural bias significantly enhances robustness in cross-domain transfer, such as from synthetic to real-world environments, where traditional pixel-wise models often fail to maintain consistency.

- We demonstrate that depth supervision induces structured representations that capture the 3D scene layout. Consequently, SHED refines semantic segmentation by ensuring that category labels strictly adhere to geometrically consistent spatial boundaries.
- Since SHED maintains a symbolic hierarchy of segments, it enables the discovery of object parts in 3D space without any part-level labels. This provides a level of structural interpretability that holistic, black-box architectures like DPT (Ranftl et al., 2021) fundamentally lack.

2. Related Work

Dense prediction is a core problem in computer vision, aiming to assign pixel-level outputs across an image (Forsyth & Ponce, 2002). It includes tasks such as semantic segmentation (Long et al., 2015), depth estimation (Eigen et al., 2014), optical flow (Teed & Deng, 2020), and image editing (Isola et al., 2017). Modern approaches typically adopt encoder-decoder architectures, such as U-Net (Ronneberger et al., 2015) and DPT (Ranftl et al., 2021), trained using task-specific supervision. These models perform well on benchmarks focused on per-pixel accuracy, as demonstrated by large-scale systems like Segment Anything (Ravi et al., 2025) and Depth Anything (Yang et al., 2024). However, recent studies show that even top-performing models often lack structural consistency (El Banani et al., 2024; Man et al., 2024). We argue that dense prediction should move beyond local estimation toward structured reasoning guided by region-level abstraction.

Monocular depth estimation is a representative dense prediction task, that infers per-pixel depth from a single image. It is widely used in 3D reconstruction (Song et al., 2017), autonomous driving (Geiger et al., 2012), and robotic perception (Tateno et al., 2017). Structural cues in depth estimation have been extensively explored to enhance geometric coherence. Existing approaches can be broadly categorized into four types: **1)** Representation approaches modify how depth is encoded, such as by discretizing depth values (Fu et al., 2018; Bhat et al., 2021; Li et al., 2024) or modeling spatial dependencies (Liu et al., 2015; Cheng et al., 2018; Yuan et al., 2022). **2)** Regularization imposes geometric constraints through loss functions that promote smooth surfaces (Godard et al., 2017; Zhan et al., 2018; Bian et al., 2019), consistent normals (Yang et al., 2018), or planar regions (Yin et al., 2019; Watson et al., 2019). **3)** Multi-task learning jointly estimates depth with auxiliary signals, such as scene geometry (Eigen & Fergus, 2015; Yin & Shi, 2018) or semantics (Mousavian et al., 2016; Kendall et al., 2018; Chen et al., 2019; Guizilini et al., 2020; Zhu et al., 2020). **4)** Post-processing refines predictions using off-the-shelf techniques (Krähenbühl & Koltun, 2011; Chen et al., 2016).

Several multi-task approaches have explored segmentation as an auxiliary signal to improve depth estimation. Early works used segmentation as an additional supervision signal (Mousavian et al., 2016; Kendall et al., 2018), while more recent ones leveraged segment regions or boundaries to guide depth discontinuities (Chen et al., 2019; Guizilini et al., 2020; Zhu et al., 2020). In contrast, SHED integrates segmentation directly into the model’s internal representation, enabling depth and segmentation to be jointly constructed and refined within a unified hierarchical framework. Moreover, the segment hierarchy in SHED is learned in an unsupervised manner, eliminating the need for additional human annotations.

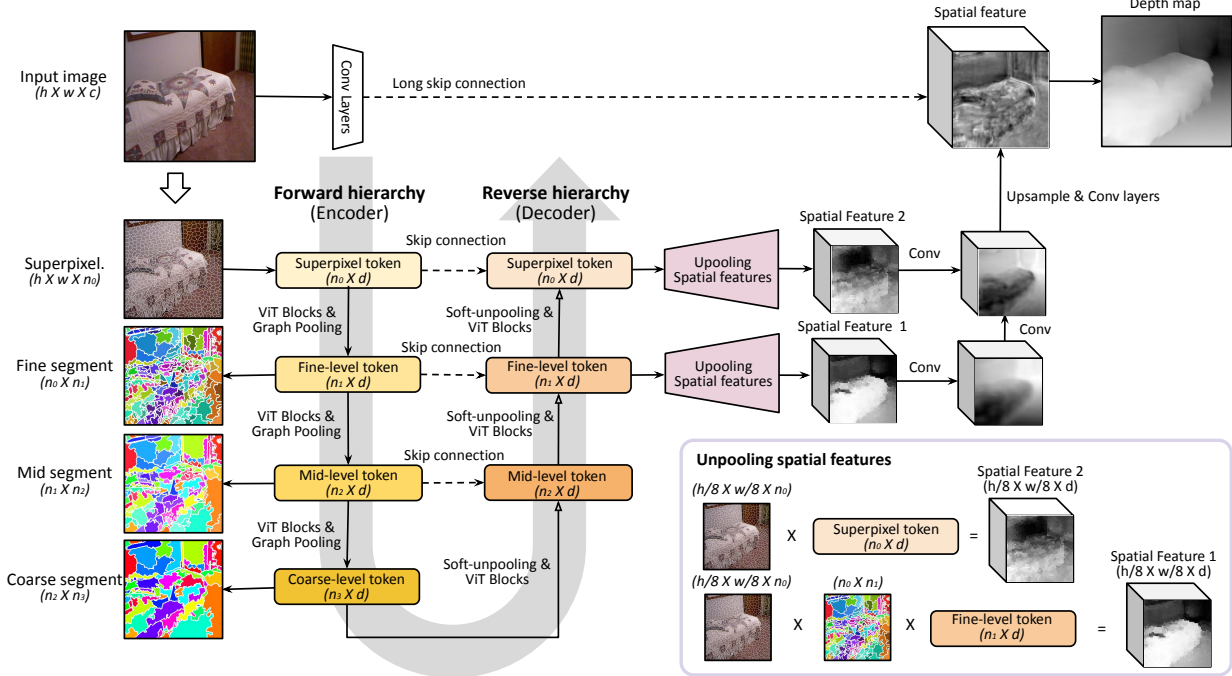


Figure 2. SHED introduces a bidirectional segment hierarchy for dense prediction. SHED decomposes dense prediction into two complementary processes: structural abstraction and structural inversion. 1) The encoder constructs a forward hierarchy by grouping superpixel tokens into increasingly abstract segments. 2) The decoder explicitly inverts this hierarchy by unpooling segment representations from coarse to fine, enabling global structural context to directly constrain pixel-level predictions. Segment tokens are projected into region-aligned 2D feature maps and fused across hierarchy levels, together with early convolutional features, to recover fine details and produce the final dense map.

Perceptual grouping is a key mechanism in human vision that organizes low-level elements into coherent global structures (Wertheimer, 1938; Marr, 2010). This principle has inspired a broad range of computer vision research, including perception (Locatello et al., 2020; Mo et al., 2021; Kang et al., 2022; Deng et al., 2023; Ranasinghe et al., 2023), segmentation (Arbeláez et al., 2012; Hwang et al., 2019; Ke et al., 2022; Xu et al., 2022), and generation (Hong et al., 2018; Mo et al., 2018; He et al., 2022). In particular, CAST (Ke et al., 2024) recently applied it to ViTs for concurrent segmentation and recognition. However, most of these methods, including CAST, consider only a *forward hierarchy*, constructing representations and segmentations in a bottom-up manner. Without a reverse hierarchy, such representations cannot enforce spatial consistency in fine-grained dense prediction. In contrast, we adopt the complementary concept of a *reverse hierarchy* (Hochstein & Ahissar, 2002), where global structures guide and refine local parts through top-down feedback. While some prior works (Anderson et al., 2018; Shi et al., 2023; Eftekhar et al., 2023) have explored reverse hierarchies for recognition, they do not address dense prediction. Other studies (Eslami et al., 2016; Sajjadi et al., 2022; Seitzer et al., 2022) apply similar ideas to encoder-decoder architectures, but focus on object-centric representations, lacking the ability to model segment hierarchies. To the best of our knowledge, this is the first work to

leverage bidirectional segment hierarchies to enhance dense prediction within a modern ViT.

3. Segment Hierarchy for Dense Prediction

We propose SHED, a dense prediction architecture that explicitly models a bidirectional segment hierarchy (see Figure 2). The encoder constructs a forward segment hierarchy that abstracts fine-grained regions into increasingly coarse structural units. This hierarchy serves as the structural backbone of SHED, capturing part-whole relationships that are difficult to represent using grid-based tokens. While similar hierarchical grouping strategies have been explored for image-level recognition, dense prediction requires such abstractions to be explicitly reversible, which motivates our overall bidirectional design.

3.1. Encoder: Grouping segments via forward hierarchy

The encoder constructs a forward segment hierarchy that abstracts fine-grained regions into increasingly coarse structural units. This hierarchy serves as the structural backbone of SHED, capturing part-whole relationships that are difficult to represent using grid-based tokens. While similar hierarchical grouping strategies have been explored for image-level recognition, dense prediction requires such abstractions to be explicitly reversible, which motivates our overall bidirectional design.

To construct the forward hierarchy, we adopt a segment-

based tokenization strategy that replaces square patch tokens with superpixel tokens and progressively clusters them based on feature similarity. This grouping mechanism follows prior work on hierarchical segmentation (Ke et al., 2024), but in SHED it serves a fundamentally different role: providing intermediate structural representations that will later be inverted for dense prediction.

Unlike encoder-only hierarchical segmentation models, the forward hierarchy in SHED is not an end in itself. Instead, it defines an intermediate structural representation whose primary purpose is to be inverted by the decoder to enable structured dense prediction.

Tokenization. Given an image $X \in \mathbb{R}^{h \times w \times c}$, the encoder produces hierarchical segmentations S_0, S_1, \dots and corresponding embeddings Z_0, Z_1, \dots , ordered from fine to coarse. This process begins by dividing the image into n_0 superpixels, which yields a one-hot assignment matrix $S_0 \in \mathbb{R}^{(h \cdot w) \times n_0}$ that maps each pixel to a superpixel. We extract a convolutional feature map $F_{\text{conv}} \in \mathbb{R}^{(h_0 \cdot w_0) \times d}$ with spatial stride 8 ($h_0 = h/8, w_0 = w/8$), add fixed sinusoidal positional embeddings, and average-pool features within each superpixel to obtain initial embeddings $Z_0 \in \mathbb{R}^{n_0 \times d}$. For global context modeling, we append a class token to form $\bar{Z}_0 \in \mathbb{R}^{(n_0+1) \times d}$, and feed it into the first ViT block.

Hierarchical clustering. Coarser segments are obtained by alternating ViT blocks and graph pooling (Ke et al., 2024). At each level l , given Z_{l-1} and S_{l-1} from the previous layer, we append a class token to form \bar{Z}_{l-1} , apply ViT blocks, and obtain updated features, excluding the class token.

To form coarser tokens $Z_l \in \mathbb{R}^{n_l \times d}$, we compute a soft assignment matrix $P_l \in \mathbb{R}^{n_{l-1} \times n_l}$ based on cosine similarity between fine- and coarse-level tokens:

$$P_l(i \rightarrow j) \propto \text{sim}(Z_{l-1}[i], Z_l[j]), \quad \text{for } i \in [n_{l-1}], j \in [n_l],$$

where $[n] := \{0, \dots, n-1\}$. The coarse tokens Z_l are initialized via farthest point sampling (Qi et al., 2017) from Z_{l-1} , and refined by aggregating fine-level features by P_l , followed by an MLP and a residual connection:

$$Z_l \leftarrow Z_l + \text{MLP}(P_l^\top Z_{l-1} \oslash P_l^\top \mathbf{1}),$$

where \oslash denotes element-wise division for normalization.

To propagate segmentation labels through the hierarchy, we compute coarser segmentations by composing the assignment matrices:

$$S_l = S_{l-1} \bar{P}_l, \quad l = 1, 2, \dots, l_{\max},$$

where \bar{P}_l is a hard assignment matrix obtained by taking the argmax over each row of P_l .

3.2. Decoder: Predicting outputs via reverse hierarchy

The decoder reconstructs spatial feature maps by reversing the encoder’s segment hierarchy, progressively unpooling

segment tokens $Z_{l_{\max}}, \dots, Z_0$. This involves two steps: **1)** computing decoder features Z'_l by unpooling from Z'_{l+1} and fusing them with encoder features Z_l via skip connections; and **2)** projecting Z'_l to the image space to obtain a spatial feature map F_l of size (h_l, w_l) .

Unpooling segment tokens. Formally, the reverse hierarchy distributes coarse segment features to finer segments through learned soft assignments. At each level $l = l_{\max} - 1, \dots, 0$, we compute

$$Z'_l \leftarrow P_{l+1}^\top Z'_{l+1},$$

which distributes coarse features to finer segments. We then add unpooled features with corresponding encoder output:

$$Z'_l \leftarrow \text{MLP}(Z'_l + Z_l),$$

followed by ViT blocks with class tokens.

Unpooling spatial features. We convert the segment tokens Z'_l into spatial feature maps by composing the soft assignment matrices:

$$P_{0 \rightarrow l} = P_1 \cdots P_l \in \mathbb{R}^{n_0 \times n_l},$$

and applying them to the initial superpixel-to-pixel map S_0 to obtain soft segmentations $S_{0 \rightarrow l} = S_0 P_{0 \rightarrow l}$. The spatial feature map is then reconstructed as

$$F_l = S_{0 \rightarrow l} Z'_l, \quad F_l \in \mathbb{R}^{(h_l \cdot w_l) \times d}.$$

The set of spatial maps $\{F_l\}_{l=1}^{l_{\max}}$ is fused using convolutional layers, combined with F_{conv} , and refined through final convolution and upsampling to produce the final dense prediction.

A common design in dense prediction is to build a spatial hierarchy by progressively reducing feature resolution. DPT (Ranftl et al., 2021) is a representative example of this approach. DPT reduces the spatial resolution of feature maps F_l at each level by a factor of 2^l , with $h_l = h_0/2^l$, $w_l = w_0/2^l$, producing coarse maps in early ViT layers that are progressively refined. However, it relies on local aggregation, which lacks structural consistency. In contrast, SHED replaces the spatial hierarchy with a segment hierarchy that explicitly models region abstraction and inversion. By operating on segment tokens rather than grid locations, SHED enforces structural consistency across hierarchy levels and within regions. Therefore, we omit spatial reduction in SHED and simply set $h_l = h_0, w_l = w_0$.

4. Experiments

We demonstrate the benefits of SHED by integrating segmentation into the loop for dense prediction: **1)** Segment-consistent depth estimation that preserves occlusion boundaries and intra-segment coherence, leading to improved accuracy and efficiency; **2)** Structure-aware representation learning through dense supervision; **3)** 3D scene reconstruction from predicted depth maps, yielding globally coherent and part-aware structures.

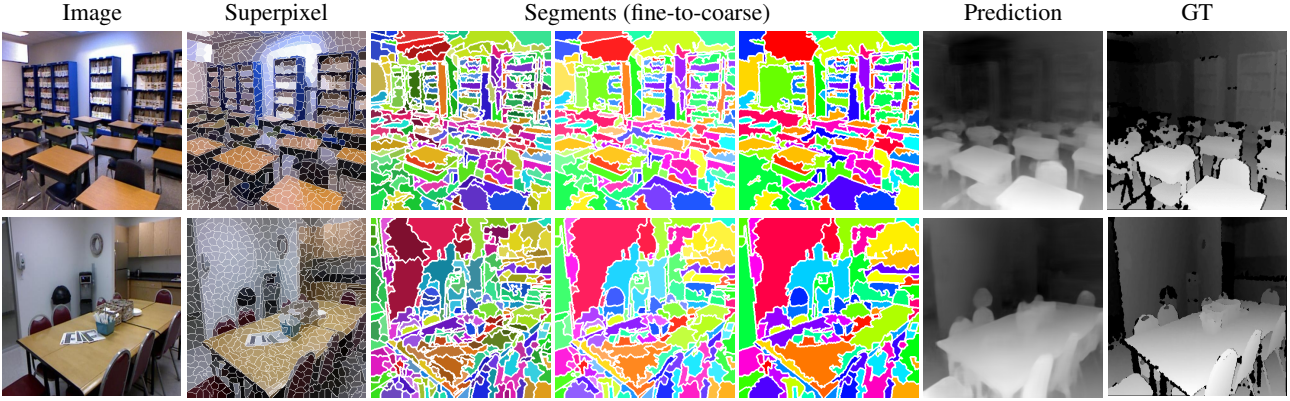


Figure 3. SHED produces consistent structures in predicted depth map with spatio-layout. We visualize the fine-to-coarse segments and corresponding depth maps from SHED, along with ground truth (GT) depth. Examples are from the NYUv2 test set. SHED captures fine structures through its segments, such as desks in a classroom, which allow the depth map to clearly separate them from the background (row 1). It also decomposes large objects, such as a table, into multiple parts, leading to smooth depth variations toward the back (row 2).

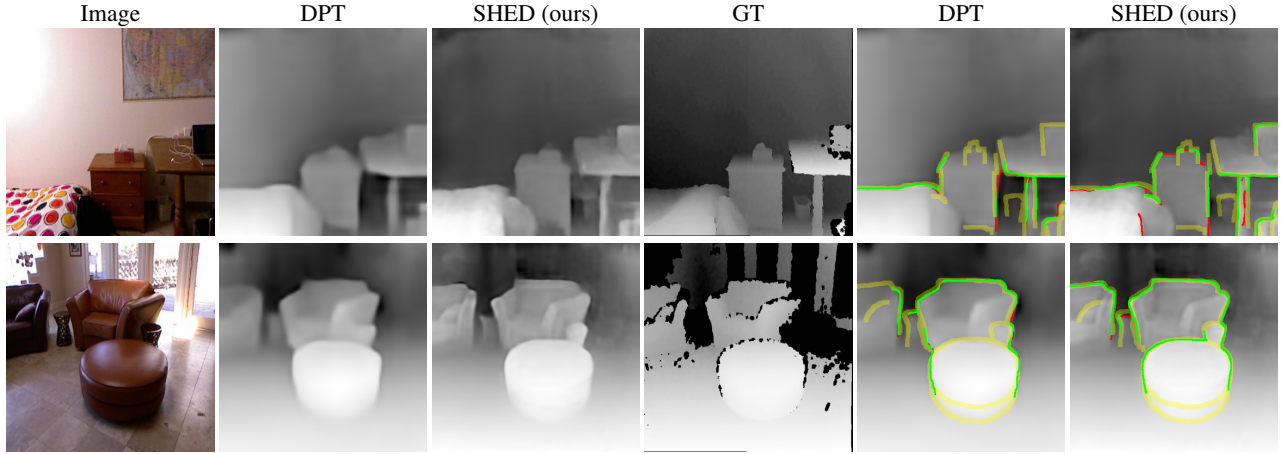


Figure 4. SHED generates sharper object contours, clearer occlusion boundaries, and more coherent values within segments. We compare depth maps (cols 2-4) and occlusion boundaries (cols 5, 6) from DPT, SHED on the NYUv2-OC++ dataset. Boundaries are extracted using a Cammy edge detector and evaluated against GT, with GT edges shown in yellow, true positive in green and false positive in red. SHED more accurately captures object edges and produces smoother depth within segments. Its predicted boundaries also align more closely with the ground truth.

4.1. Setup

For fair comparison with prior dense prediction methods, we follow the standard training protocol commonly used in DPT-style models (Ranftl et al., 2021). Specifically, we adopt the DPT-Hybrid configuration, which combines ResNet-50 (He et al., 2016) and ViT-Small (Dosovitskiy, 2020), and refer to it simply as DPT throughout the paper. For in-domain evaluation, we primarily train and evaluate on NYUv2 (Nathan Silberman & Fergus, 2012), a standard benchmark for indoor depth estimation. For cross-domain transfer, we train SHED on the synthetic HyperSim dataset (Roberts et al., 2021) and assess its zero-shot generalization on the real-world NYUv2 dataset. We further compare our approach with stronger prior-based models, including the DPT-style Depth Anything v2 (Yang et al., 2024) and Marigold (Ke et al., 2025), both fine-tuned on HyperSim. Depth Anything v2 uses the DPT decoder with

DINOv2 (Oquab et al., 2023) encoder.

Tokenization. Input images of size 640×480 are randomly cropped to 384×384 during preprocessing. We generate 576 superpixels using the SEEDS algorithm (Van den Bergh et al., 2012), matching the 24×24 token grid of DPT, which corresponds to 16×16 patches. Features are extracted from intermediate ResNet-50 blocks at 1/4 and 1/8 of the input resolution; the latter initializes segment token embeddings, while both are passed to the final decoder via skip connections. This entire preprocessing and tokenization pipeline is applied consistently in all experiments.

Architecture. With graph pooling and unpooling layers, the encoder consists of three stages, each with two ViT blocks followed by graph pooling, progressively reducing the number of segment tokens to 256, 128, and 64. The decoder mirrors this with unpooling and receives skip connections from the corresponding encoder stages.

Table 1. SHED improves boundary accuracy and object-level consistency. We evaluate the structural quality of depth maps using two metrics: 1) Occlusion boundary error, evaluated on the NYUv2-OC++ dataset. Occlusion boundaries are extracted using a Canny edge detector, and the Chamfer distance is computed in both directions: from prediction to ground truth and vice versa. 2) Intra-segment coherence measures how well the predicted depth values within each object align with the ground-truth using object-level annotations.

Method	Boundary Error ↓		Object-wise Depth Accuracy ↑		Object-wise Depth Error ↓		
	ϵ_a	ϵ_c	$\delta > 1.25$	$\delta > 1.25$	AbsRel	RMSE	log 10
DPT	6.395	1.438		0.802	0.144	0.500	0.061
SHED (ours)	5.713	0.608		0.814	0.142	0.496	0.060

Table 2. SHED achieves competitive in-domain performance and strong cross-domain generalization (synthetic → real). We report accuracy and error metrics on the NYUv2 test set, comparing SHED against classical baselines and modern learning-based methods. Notably, SHED not only yields in-domain results comparable to DPT but also demonstrates competitive zero-shot generalization from synthetic to real data, matching the robustness of Depth Anything v2 (Yang et al., 2024) and Marigold (Ke et al., 2025).

Method	Pre-training	Training	Depth Accuracy			Depth Error		
			$\delta > 1.25 \uparrow$	$\delta > 1.25^2 \uparrow$	$\delta > 1.25^3 \uparrow$	AbsRel ↓	RMSE ↓	log10 ↓
<i>In-domain depth estimation (trained on NYUv2)</i>								
DPT	IN-1K	NYUv2	0.839	0.971	0.992	0.132	0.457	0.055
SHED (ours)	IN-1K	NYUv2	0.846	0.972	0.992	0.130	0.451	0.054
<i>Joint segmentation-depth learning</i>								
Mousavian et al. (Mousavian et al., 2016)	IN-1K	NYUv2	0.568	0.856	0.956	0.200	0.816	0.061
Simsar et al. (Simsar et al., 2022)	IN-1K	NYUv2	0.847	0.971	0.993	0.116	0.448	-
SHED (ours)	IN-1K	NYUv2	0.855	0.974	0.993	0.123	0.433	0.052
<i>Cross-domain zero-shot depth estimation (HyperSim → NYUv2)</i>								
Marigold (Ke et al., 2025)	Laion-5b	HyperSim	0.375	0.659	0.833	0.542	1.243	0.171
Depth Anything v2 (Yang et al., 2024)	LVM-142M	HyperSim	0.592	0.902	0.960	0.749	0.808	0.110
SHED (ours)	IN-1K	HyperSim	0.632	0.892	0.960	0.583	0.740	0.102

Table 3. Ablation study of hierarchical encoding and decoding in SHED. We compare the full model with a variant that removes the reverse hierarchy in the decoder on the NYUv2 test set. The results highlight the role of coarse-to-fine unpooling in depth prediction.

Method	Depth Accuracy			Depth Error		
	$\delta > 1.25 \uparrow$	$\delta > 1.25^2 \uparrow$	$\delta > 1.25^3 \uparrow$	AbsRel ↓	RMSE ↓	log10 ↓
DPT	0.839	0.971	0.992	0.132	0.457	0.055
SHED with forward hierarchy only	0.755	0.951	0.989	0.163	0.552	0.069
SHED (ours)	0.846	0.972	0.992	0.130	0.451	0.054

We train SHED and DPT on NYUv2 using a batch size of 16 for 50 epochs with the Adam optimizer (Kingma & Ba, 2014) and a learning rate of 5e-5. With pretrained ResNet and ViT backbones, we follow DPT’s default training recipe, including the scale-invariant logarithmic loss computed against ground-truth depth. At inference time, predicted depth maps at 384×384 resolution are bilinearly upsampled to 640×480 to match the ground-truth size.

4.2. Segment-consistent depth estimation

SHED generates structured depth maps using a learned segment hierarchy. We first visualize this structural alignment, then evaluate boundary quality and coherence, and finally demonstrate that this hierarchical approach improves per-pixel metrics and efficiency. Figure 3 shows how the segment hierarchy in SHED benefits geometry. The learned segments capture contours of objects, such as desks in a classroom, allowing the depth to clearly separate them from the floor. They also decompose larger structures, like tables, into parts, enabling smooth depth transitions from front to

back. This suggests that structure guides depth prediction toward more accurate and interpretable results.

Boundary accuracy. We assess the structural quality of SHED by comparing occlusion boundaries against DPT on the NYUv2-OC++ dataset (Ramamonjisoa et al., 2020). Figure 4 shows predicted depth maps and their occlusion boundaries, extracted using a Canny edge detector (Canny, 1986). For quantitative evaluation, we follow the standard protocol (Koch et al., 2018) and compute the average Chamfer distance (Fan et al., 2017) in two directions: from prediction to ground truth, and vice versa. SHED produces sharper contours and outperforms DPT on both metrics with its fine-grained segmentation.

Intra-segment coherence. Beyond boundary, we evaluate how coherently depth values vary within each segment. We employ object-wise depth accuracy and error, treating ground-truth semantic segmentation masks as structural references on NYUv2 (Nathan Silberman & Fergus, 2012). As shown in Figure 4, SHED produces smoother depth vari-

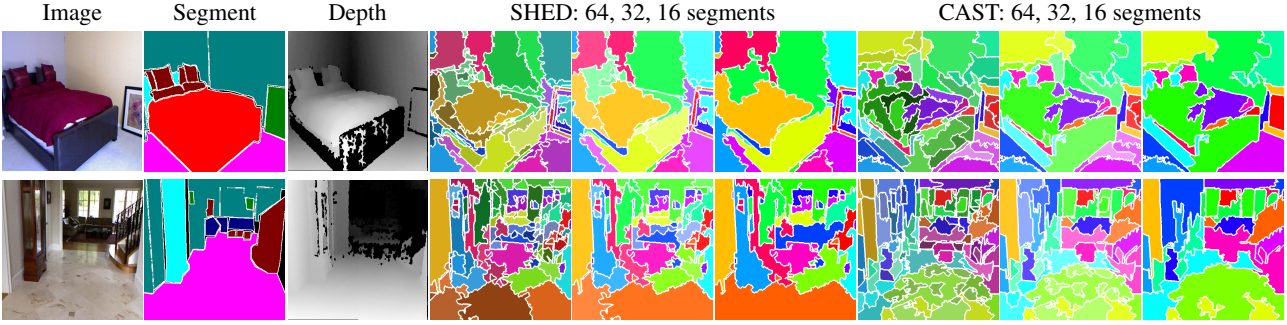


Figure 5. SHED learns depth-aware segment hierarchies, while CAST relies on visual cues. We compare segmentations from SHED and CAST (Ke et al., 2024) at the same hierarchy levels: 64, 32, and 16 segments. SHED captures meaningful part structures, such as separating the blanket and pillow from the bed (row 1). It also decomposes large structures like the floor based on depth, grouping nearby regions into a single large segment while dividing distant areas into smaller ones (row 2). In contrast, CAST relies on appearance cues and fails to capture geometric structure. For instance, it groups white floor regions by color but divides them arbitrarily, ignoring depth. These results highlight the value of depth supervision in learning 3D-aware segmentations.

ations within segments. This is reflected quantitatively in Table 1. SHED achieves lower error and higher accuracy within segments, confirming that our hierarchical pooling promotes smoother and more coherent depth predictions.

Per-pixel metrics & generalization. Table 2 reports standard per-pixel depth metrics under both in-domain and cross-domain settings. Under in-domain evaluation on NYUv2, SHED outperforms the DPT baseline and prior approaches that incorporate segmentation cues for depth estimation. For example, methods such as (Simsar et al., 2022) enforce object-level consistency via over-segmentation, while multi-task frameworks like (Mousavian et al., 2016) jointly supervise semantics and depth. The benefits of structural modeling become pronounced under cross-domain evaluation. Despite relying only on ImageNet pre-training, SHED exhibits strong zero-shot generalization from HyperSim to NYUv2, outperforming large-scale foundation models on most metrics. In particular, it surpasses Depth Anything v2 (Yang et al., 2024), which leverages a DINOv2 (Oquab et al., 2023) encoder, and Marigold (Ke et al., 2025), pre-trained on billions of images. These results suggest that incorporating explicit structural constraints offers a data-efficient path to robust depth estimation across domains. We report results on a diverse set of benchmarks in Section C.

Computational efficiency. For a fair and hardware-independent comparison of structural complexity, we report both the number of parameters and the computational cost in FLOPs. DPT-Hybrid contains 41.88 million parameters and requires 135.0 GFLOPs. In contrast, SHED uses 56.58 million parameters but reduces the computation to 103.2 GFLOPs, which is approximately a **24% decrease in FLOPs**. This substantial reduction demonstrates that SHED is structurally more efficient and achieves lower theoretical latency despite having a slightly larger parameter count.

Ablation. We conducted an ablation study to isolate the contributions of the hierarchical clustering in the encoder

Table 5. Semantic segmentation comparison results on ADE20K. Segment hierarchies learned by SHED improve alignment with semantic regions and boundaries on ADE20K.

Method	mIoU	boundary F-score
CAST	43.1	36.5
SHED (ours)	44.5	37.7

and the hierarchy reversing in the decoder. To verify the necessity of our proposed decoder, we experimented with a variant of SHED by removing the progressive unpooling process in the decoder. Table 3 shows removing the reverse hierarchy leads to a sharp performance degradation, falling significantly behind the DPT baseline. This demonstrates that the coarse-to-fine unpooling mechanism in the decoder is essential to recover fine-grained spatial details from the grouped representations.

4.3. Structure-aware representation learning

Depth-aware image segmentation. We analyze the segment hierarchy learned by SHED by comparing it to CAST, an encoder trained for image recognition using segment-based representations. Specifically, we use CAST, trained on ImageNet (Deng et al., 2009) with the MoCo-v3 objective (Chen et al., 2021), a self-supervised learning by instance discrimination (Wu et al., 2018) that clusters visually similar images. To ensure a fair comparison, we adapt the graph pooling layers of SHED to generate the same number of segments (64, 32, and 16) from 196 superpixels at a 224×224 resolution.

Figure 5 shows that SHED learns hierarchical structures that align with scene geometry. It separates objects like blankets and decomposes large structures such as floors into segments that reflect their spatial extent. In contrast, CAST groups regions based on appearance. For example, it clusters white floor areas by color but fails to account for geometric cues. We attribute this difference to the training objective. CAST learns segments through image-level recognition,

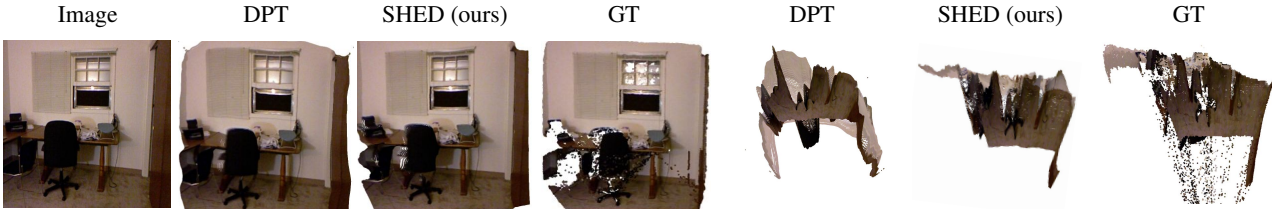


Figure 6. SHED produces structured 3D reconstructions. We visualize 3D point clouds reconstructed from single-view depth maps, following the semantic scene completion protocol (Song et al., 2017), using predictions from DPT, SHED, and the ground truth on NYUv2 examples. Frontal views (cols 2-4) show that DPT fails to preserve planar structures, producing curved wall boundaries, whereas SHED more accurately recovers straight lines. This difference is more apparent in the bird’s-eye views (cols 5-7): DPT yields warped surfaces, while SHED produces flatter layouts.

Table 4. 3D alignment induced by structured depth estimation. We compute the Chamfer distance between point clouds from the predicted and ground-truth depths. SHED achieves lower errors than DPT, indicating improved geometric alignment.

Method	Precision / Recall ↓
DPT	0.171 / 0.251
SHED (ours)	0.158 / 0.244

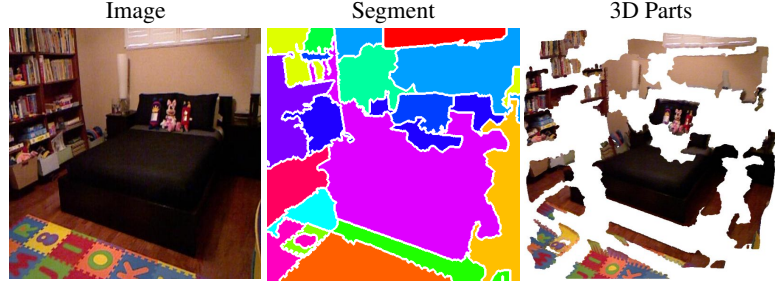


Figure 7. SHED discovers 3D part structures. Concurrent segmentation and depth estimation enable part-level decomposition of the 3D point clouds.

while SHED is guided by dense prediction.

Semantic segmentation. We further evaluate whether the learned segment hierarchies align with semantic structures on the ADE20K dataset (Zhou et al., 2017). Following the CAST evaluation protocol, we report region-level mean IoU and boundary F-score between the predicted segments and ground-truth annotations. As shown in Table 5, SHED consistently outperforms CAST on both metrics. Notably, this improvement cannot be attributed solely to encoder pre-training. While both models leverage segment hierarchy, SHED incorporates a hierarchical decoding pipeline that progressively reverses the segment hierarchy, enabling fine-grained spatial details to be recovered from grouped representations. This coarse-to-fine decoding process facilitates more accurate alignment with semantic boundaries, leading to improved segmentation quality without requiring explicit semantic supervision.

4.4. 3D scene reconstruction with part structures

We demonstrate SHED’s capability for 3D scene understanding. While plausible pixel values may suffice for 2D depth estimation, accurate and structured depth is particularly critical when projected into 3D space. Accordingly, SHED enables high-quality 3D reconstruction and supports unsupervised 3D part discovery through segmentation. To evaluate the structural quality of depth maps, we project them into 3D point clouds on the NYUv2 dataset (Nathan Silberman & Fergus, 2012), following the semantic scene completion protocol (Song et al., 2017) and using NYUv2 camera in-

trinsics. For interpretability, all depth values are scaled by 1/1000. Figure 6 shows that SHED produces cleaner reconstructions with sharper boundaries and flatter surfaces that better align with ground truth geometry, whereas DPT yields curvier, less faithful shapes. We quantify reconstruction performance with the Chamfer distance (Fan et al., 2017) in both directions. Table 4 shows that SHED consistently achieves lower distances than DPT, confirming its advantage in structured 3D prediction. By jointly predicting segmentation and depth, SHED lifts 2D parts into 3D space, enabling part-level decomposition of scenes.

Figure 7 shows an example from NYUv2, where segments corresponding to objects form coherent 3D structures in point clouds. This demonstrates SHED’s potential for unsupervised 3D part reasoning, a key capability for interactive and dynamic scene understanding (Mo et al., 2019).

5. Conclusion

We shed light on the role of segmentation in depth estimation. SHED learns a segment hierarchy in the encoder and reverses it in the decoder to predict dense maps. This results in depth maps with segment-consistent structure, structure-aware representations, and coherent 3D scenes with interpretable parts. Our principle of unifying reconstruction and reorganization offers a new direction for 3D vision and robotics, particularly for tasks that require fine-grained interaction with physical components. Additional results and limitations are discussed in Section E.

Impact statement. This research was conducted responsibly based on the principles outlined in the ICML Code of Ethics. This technology can enhance the 3D environmental perception of autonomous driving systems, thereby improving road safety, and can help robots interact more safely and efficiently with their surroundings. Before deploying this model in real-world scenarios, it must undergo rigorous and thorough validation for robustness and safety across a wide range of conditions.

References

Anderson, P., He, X., Buehler, C., Teney, D., Johnson, M., Gould, S., and Zhang, L. Bottom-up and top-down attention for image captioning and visual question answering. In *Proceedings of the IEEE conference on computer vision and pattern recognition*, pp. 6077–6086, 2018.

Arbeláez, P., Hariharan, B., Gu, C., Gupta, S., Bourdev, L., and Malik, J. Semantic segmentation using regions and parts. In *2012 IEEE conference on computer vision and pattern recognition*, pp. 3378–3385. IEEE, 2012.

Bhat, S. F., Alhashim, I., and Wonka, P. Adabins: Depth estimation using adaptive bins. In *Proceedings of the IEEE/CVF conference on computer vision and pattern recognition*, pp. 4009–4018, 2021.

Bian, J., Li, Z., Wang, N., Zhan, H., Shen, C., Cheng, M.-M., and Reid, I. Unsupervised scale-consistent depth and ego-motion learning from monocular video. *Advances in neural information processing systems*, 32, 2019.

Cabon, Y., Murray, N., and Humenberger, M. Virtual kitti 2. *arXiv preprint arXiv:2001.10773*, 2020.

Canny, J. A computational approach to edge detection. *IEEE Transactions on pattern analysis and machine intelligence*, (6):679–698, 1986.

Chen, P.-Y., Liu, A. H., Liu, Y.-C., and Wang, Y.-C. F. Towards scene understanding: Unsupervised monocular depth estimation with semantic-aware representation. In *Proceedings of the IEEE/CVF Conference on computer vision and pattern recognition*, pp. 2624–2632, 2019.

Chen, W., Fu, Z., Yang, D., and Deng, J. Single-image depth perception in the wild. *Advances in neural information processing systems*, 29, 2016.

Chen, X., Xie, S., and He, K. An empirical study of training self-supervised vision transformers. In *Proceedings of the IEEE/CVF international conference on computer vision*, pp. 9640–9649, 2021.

Cheng, X., Wang, P., and Yang, R. Depth estimation via affinity learned with convolutional spatial propagation network. In *Proceedings of the European conference on computer vision (ECCV)*, pp. 103–119, 2018.

Deng, J., Dong, W., Socher, R., Li, L.-J., Li, K., and Fei-Fei, L. Imagenet: A large-scale hierarchical image database. In *2009 IEEE conference on computer vision and pattern recognition*, pp. 248–255. Ieee, 2009.

Deng, Z., Chen, T., and Li, Y. Perceptual group tokenizer: Building perception with iterative grouping. *arXiv preprint arXiv:2311.18296*, 2023.

Dosovitskiy, A. An image is worth 16x16 words: Transformers for image recognition at scale. *arXiv preprint arXiv:2010.11929*, 2020.

Eftekhari, A., Zeng, K.-H., Duan, J., Farhadi, A., Kembhavi, A., and Krishna, R. Selective visual representations improve convergence and generalization for embodied ai. *arXiv preprint arXiv:2311.04193*, 2023.

Eigen, D. and Fergus, R. Predicting depth, surface normals and semantic labels with a common multi-scale convolutional architecture. In *Proceedings of the IEEE international conference on computer vision*, pp. 2650–2658, 2015.

Eigen, D., Puhrsch, C., and Fergus, R. Depth map prediction from a single image using a multi-scale deep network. *Advances in neural information processing systems*, 27, 2014.

El Banani, M., Raj, A., Maninis, K.-K., Kar, A., Li, Y., Rubinstein, M., Sun, D., Guibas, L., Johnson, J., and Jampani, V. Probing the 3d awareness of visual foundation models. In *Proceedings of the IEEE/CVF Conference on Computer Vision and Pattern Recognition*, pp. 21795–21806, 2024.

Eslami, S., Heess, N., Weber, T., Tassa, Y., Szepesvari, D., Hinton, G. E., et al. Attend, infer, repeat: Fast scene understanding with generative models. *Advances in neural information processing systems*, 29, 2016.

Fan, H., Su, H., and Guibas, L. J. A point set generation network for 3d object reconstruction from a single image. In *Proceedings of the IEEE conference on computer vision and pattern recognition*, pp. 605–613, 2017.

Forsyth, D. A. and Ponce, J. *Computer vision: a modern approach*. prentice hall professional technical reference, 2002.

Fu, H., Gong, M., Wang, C., Batmanghelich, K., and Tao, D. Deep ordinal regression network for monocular depth estimation. In *Proceedings of the IEEE conference on computer vision and pattern recognition*, pp. 2002–2011, 2018.

Geiger, A., Lenz, P., and Urtasun, R. Are we ready for autonomous driving? the kitti vision benchmark suite. In *2012 IEEE conference on computer vision and pattern recognition*, pp. 3354–3361. IEEE, 2012.

Geiger, A., Lenz, P., Stiller, C., and Urtasun, R. Vision meets robotics: The kitti dataset. *The international journal of robotics research*, 32(11):1231–1237, 2013.

Godard, C., Mac Aodha, O., and Brostow, G. J. Unsupervised monocular depth estimation with left-right consistency. In *Proceedings of the IEEE conference on computer vision and pattern recognition*, pp. 270–279, 2017.

Guizilini, V., Hou, R., Li, J., Ambrus, R., and Gaidon, A. Semantically-guided representation learning for self-supervised monocular depth. *arXiv preprint arXiv:2002.12319*, 2020.

He, K., Zhang, X., Ren, S., and Sun, J. Deep residual learning for image recognition. In *Proceedings of the IEEE conference on computer vision and pattern recognition*, pp. 770–778, 2016.

He, X., Wandt, B., and Rhodin, H. Ganseg: Learning to segment by unsupervised hierarchical image generation. In *Proceedings of the IEEE/CVF Conference on Computer Vision and Pattern Recognition*, pp. 1225–1235, 2022.

Hochstein, S. and Ahissar, M. View from the top: Hierarchies and reverse hierarchies in the visual system. *Neuron*, 36(5):791–804, 2002.

Hong, S., Yang, D., Choi, J., and Lee, H. Inferring semantic layout for hierarchical text-to-image synthesis. In *Proceedings of the IEEE conference on computer vision and pattern recognition*, pp. 7986–7994, 2018.

Hwang, J.-J., Yu, S. X., Shi, J., Collins, M. D., Yang, T.-J., Zhang, X., and Chen, L.-C. Segsort: Segmentation by discriminative sorting of segments. In *Proceedings of the IEEE/CVF International Conference on Computer Vision*, pp. 7334–7344, 2019.

Isola, P., Zhu, J.-Y., Zhou, T., and Efros, A. A. Image-to-image translation with conditional adversarial networks. In *Proceedings of the IEEE conference on computer vision and pattern recognition*, pp. 1125–1134, 2017.

Kang, H., Mo, S., and Shin, J. Oamixer: Object-aware mixing layer for vision transformers. *arXiv preprint arXiv:2212.06595*, 2022.

Ke, B., Qu, K., Wang, T., Metzger, N., Huang, S., Li, B., Obukhov, A., and Schindler, K. Marigold: Affordable adaptation of diffusion-based image generators for image analysis. *arXiv preprint arXiv:2505.09358*, 2025.

Ke, T.-W., Hwang, J.-J., Guo, Y., Wang, X., and Yu, S. X. Unsupervised hierarchical semantic segmentation with multiview cosegmentation and clustering transformers. In *Proceedings of the IEEE/CVF Conference on Computer Vision and Pattern Recognition*, pp. 2571–2581, 2022.

Ke, T.-W., Mo, S., and Stella, X. Y. Learning hierarchical image segmentation for recognition and by recognition. In *The Twelfth International Conference on Learning Representations*, 2024.

Kendall, A., Gal, Y., and Cipolla, R. Multi-task learning using uncertainty to weigh losses for scene geometry and semantics. In *Proceedings of the IEEE conference on computer vision and pattern recognition*, pp. 7482–7491, 2018.

Kingma, D. P. and Ba, J. Adam: A method for stochastic optimization. *arXiv preprint arXiv:1412.6980*, 2014.

Koch, T., Liebel, L., Fraundorfer, F., and Korner, M. Evaluation of cnn-based single-image depth estimation methods. In *Proceedings of the European Conference on Computer Vision (ECCV) Workshops*, pp. 0–0, 2018.

Krähenbühl, P. and Koltun, V. Efficient inference in fully connected crfs with gaussian edge potentials. *Advances in neural information processing systems*, 24, 2011.

Li, Z. and Snavely, N. Megadepth: Learning single-view depth prediction from internet photos. In *Proceedings of the IEEE conference on computer vision and pattern recognition*, pp. 2041–2050, 2018.

Li, Z., Wang, X., Liu, X., and Jiang, J. Binsformer: Revisiting adaptive bins for monocular depth estimation. *IEEE Transactions on Image Processing*, 2024.

Liu, F., Shen, C., Lin, G., and Reid, I. Learning depth from single monocular images using deep convolutional neural fields. *IEEE transactions on pattern analysis and machine intelligence*, 38(10):2024–2039, 2015.

Liu, M., Chen, Z., Cheng, X., Ji, Y., Qiu, R.-Z., Yang, R., and Wang, X. Visual whole-body control for legged locomotion. *arXiv preprint arXiv:2403.16967*, 2024.

Locatello, F., Weissenborn, D., Unterthiner, T., Mahendran, A., Heigold, G., Uszkoreit, J., Dosovitskiy, A., and Kipf, T. Object-centric learning with slot attention. *Advances in neural information processing systems*, 33:11525–11538, 2020.

Long, J., Shelhamer, E., and Darrell, T. Fully convolutional networks for semantic segmentation. In *Proceedings of the IEEE conference on computer vision and pattern recognition*, pp. 3431–3440, 2015.

Man, Y., Zheng, S., Bao, Z., Hebert, M., Gui, L., and Wang, Y.-X. Lexicon3d: Probing visual foundation models for complex 3d scene understanding. *Advances in Neural Information Processing Systems*, 37:76819–76847, 2024.

Marr, D. *Vision: A computational investigation into the human representation and processing of visual information*. MIT press, 2010.

Mo, K., Zhu, S., Chang, A. X., Yi, L., Tripathi, S., Guibas, L. J., and Su, H. Partnet: A large-scale benchmark for fine-grained and hierarchical part-level 3d object understanding. In *Proceedings of the IEEE/CVF conference on computer vision and pattern recognition*, pp. 909–918, 2019.

Mo, S., Cho, M., and Shin, J. Instagan: Instance-aware image-to-image translation. *arXiv preprint arXiv:1812.10889*, 2018.

Mo, S., Kang, H., Sohn, K., Li, C.-L., and Shin, J. Object-aware contrastive learning for debiased scene representation. *Advances in Neural Information Processing Systems*, 34:12251–12264, 2021.

Mousavian, A., Pirsavash, H., and Košecká, J. Joint semantic segmentation and depth estimation with deep convolutional networks. In *2016 Fourth International Conference on 3D Vision (3DV)*, pp. 611–619. IEEE, 2016.

Nathan Silberman, Derek Hoiem, P. K. and Fergus, R. Indoor segmentation and support inference from rgbd images. In *ECCV*, 2012.

Quab, M., Darcer, T., Moutakanni, T., Vo, H., Szafraniec, M., Khalidov, V., Fernandez, P., Haziza, D., Massa, F., El-Nouby, A., et al. Dinov2: Learning robust visual features without supervision. *arXiv preprint arXiv:2304.07193*, 2023.

Qi, C. R., Yi, L., Su, H., and Guibas, L. J. Pointnet++: Deep hierarchical feature learning on point sets in a metric space. *Advances in neural information processing systems*, 30, 2017.

Ramamonjisoa, M., Du, Y., and Lepetit, V. Predicting sharp and accurate occlusion boundaries in monocular depth estimation using displacement fields. In *Proceedings of the IEEE/CVF Conference on Computer Vision and Pattern Recognition*, pp. 14648–14657, 2020.

Ranasinghe, K., McKinzie, B., Ravi, S., Yang, Y., Toshev, A., and Shlens, J. Perceptual grouping in contrastive vision-language models. In *Proceedings of the IEEE/CVF International Conference on Computer Vision*, pp. 5571–5584, 2023.

Ranftl, R., Bochkovskiy, A., and Koltun, V. Vision transformers for dense prediction. In *Proceedings of the IEEE/CVF international conference on computer vision*, pp. 12179–12188, 2021.

Ravi, N., Gabeur, V., Hu, Y.-T., Hu, R., Ryali, C., Ma, T., Khedr, H., Rädl, R., Rolland, C., Gustafson, L., et al. Sam 2: Segment anything in images and videos. In *ICLR*, 2025.

Roberts, M., Ramapuram, J., Ranjan, A., Kumar, A., Bautista, M. A., Paczan, N., Webb, R., and Susskind, J. M. Hypersim: A photorealistic synthetic dataset for holistic indoor scene understanding. In *Proceedings of the IEEE/CVF international conference on computer vision*, pp. 10912–10922, 2021.

Ronneberger, O., Fischer, P., and Brox, T. U-net: Convolutional networks for biomedical image segmentation. In *Medical image computing and computer-assisted intervention–MICCAI 2015: 18th international conference, Munich, Germany, October 5–9, 2015, proceedings, part III 18*, pp. 234–241. Springer, 2015.

Sajjadi, M. S., Duckworth, D., Mahendran, A., Van Steenkiste, S., Pavetic, F., Lucic, M., Guibas, L. J., Greff, K., and Kipf, T. Object scene representation transformer. *Advances in neural information processing systems*, 35:9512–9524, 2022.

Seitzer, M., Horn, M., Zadaianchuk, A., Zietlow, D., Xiao, T., Simon-Gabriel, C.-J., He, T., Zhang, Z., Schölkopf, B., Brox, T., et al. Bridging the gap to real-world object-centric learning. *arXiv preprint arXiv:2209.14860*, 2022.

Shi, B., Darrell, T., and Wang, X. Top-down visual attention from analysis by synthesis. In *Proceedings of the IEEE/CVF conference on computer vision and pattern recognition*, pp. 2102–2112, 2023.

Simsar, E., Örnek, E. P., Manhardt, F., Dhamo, H., Navab, N., and Tombari, F. Object-aware monocular depth prediction with instance convolutions. *IEEE Robotics and Automation Letters*, 7(2):5389–5396, 2022.

Song, S., Lichtenberg, S. P., and Xiao, J. Sun rgbd: A rgbd scene understanding benchmark suite. In *Proceedings of the IEEE conference on computer vision and pattern recognition*, pp. 567–576, 2015.

Song, S., Yu, F., Zeng, A., Chang, A. X., Savva, M., and Funkhouser, T. Semantic scene completion from a single depth image. In *Proceedings of the IEEE conference on computer vision and pattern recognition*, pp. 1746–1754, 2017.

Tateno, K., Tombari, F., Laina, I., and Navab, N. Cnn-slam: Real-time dense monocular slam with learned depth prediction. In *Proceedings of the IEEE conference on computer vision and pattern recognition*, pp. 6243–6252, 2017.

Teed, Z. and Deng, J. Raft: Recurrent all-pairs field transforms for optical flow. In *Computer Vision–ECCV 2020: 16th European Conference, Glasgow, UK, August 23–28, 2020, Proceedings, Part II 16*, pp. 402–419. Springer, 2020.

Van den Bergh, M., Boix, X., Roig, G., De Capitani, B., and Van Gool, L. Seeds: Superpixels extracted via energy-driven sampling. In *Computer Vision–ECCV 2012: 12th European Conference on Computer Vision, Florence, Italy, October 7–13, 2012, Proceedings, Part VII 12*, pp. 13–26. Springer, 2012.

Watson, J., Firman, M., Brostow, G. J., and Turmukhametov, D. Self-supervised monocular depth hints. In *Proceedings of the IEEE/CVF international conference on computer vision*, pp. 2162–2171, 2019.

Wertheimer, M. Laws of organization in perceptual forms. 1938.

Wu, Z., Xiong, Y., Yu, S. X., and Lin, D. Unsupervised feature learning via non-parametric instance discrimination. In *Proceedings of the IEEE conference on computer vision and pattern recognition*, pp. 3733–3742, 2018.

Xu, J., De Mello, S., Liu, S., Byeon, W., Breuel, T., Kautz, J., and Wang, X. Groupvit: Semantic segmentation emerges from text supervision. In *Proceedings of the IEEE/CVF conference on computer vision and pattern recognition*, pp. 18134–18144, 2022.

Yang, L., Kang, B., Huang, Z., Zhao, Z., Xu, X., Feng, J., and Zhao, H. Depth anything v2. *arXiv preprint arXiv:2406.09414*, 2024.

Yang, Z., Wang, P., Xu, W., Zhao, L., and Nevatia, R. Unsupervised learning of geometry from videos with edge-aware depth-normal consistency. In *Proceedings of the AAAI Conference on Artificial Intelligence*, volume 32, 2018.

Yin, W., Liu, Y., Shen, C., and Yan, Y. Enforcing geometric constraints of virtual normal for depth prediction. In *Proceedings of the IEEE/CVF international conference on computer vision*, pp. 5684–5693, 2019.

Yin, Z. and Shi, J. Geonet: Unsupervised learning of dense depth, optical flow and camera pose. In *Proceedings of the IEEE conference on computer vision and pattern recognition*, pp. 1983–1992, 2018.

Yuan, W., Gu, X., Dai, Z., Zhu, S., and Tan, P. Neural window fully-connected crfs for monocular depth estimation. In *Proceedings of the IEEE/CVF conference on computer vision and pattern recognition*, pp. 3916–3925, 2022.

Zhan, H., Garg, R., Weerasekera, C. S., Li, K., Agarwal, H., and Reid, I. Unsupervised learning of monocular depth estimation and visual odometry with deep feature reconstruction. In *Proceedings of the IEEE conference on computer vision and pattern recognition*, pp. 340–349, 2018.

Zhou, B., Zhao, H., Puig, X., Fidler, S., Barriuso, A., and Torralba, A. Scene parsing through ade20k dataset. In *Proceedings of the IEEE conference on computer vision and pattern recognition*, pp. 633–641, 2017.

Zhu, S., Brazil, G., and Liu, X. The edge of depth: Explicit constraints between segmentation and depth. In *Proceedings of the IEEE/CVF conference on computer vision and pattern recognition*, pp. 13116–13125, 2020.

A. Implementation Details

A.1. Training details

We train our model on the NYUv2 dataset (Nathan Silberman & Fergus, 2012) using the official training split. Each RGB image is first cropped to remove invalid boundaries (coordinates: 43, 45, 608, 472), then resized to 384×384 resolution. The corresponding depth maps undergo the same spatial preprocessing and are normalized by dividing raw depth values by 1000.

For data augmentation, we apply horizontal flipping with a probability of 0.5, gamma correction with $\gamma \in [0.9, 1.1]$, brightness scaling using a random factor from $[0.75, 1.25]$, and per-channel color jittering with multiplicative factors in $[0.9, 1.1]$. After augmentation, random spatial crops of size 384×384 are applied to both images and depth maps.

For tokenization, we generate superpixels using OpenCV’s SEEDS (Van den Bergh et al., 2012) algorithm. Each image is segmented into 676 superpixels using a single-level hierarchy (num_levels=1) and a histogram bin size of 5. The algorithm is run for 50 iterations to refine superpixel boundaries.

A.2. Evaluation details

We evaluate on the official NYUv2 (Nathan Silberman & Fergus, 2012) test split, which contains 654 images. All evaluations use an input resolution of 384×384 pixels, with depth values clamped to the range $[10^{-3}, 10.0]$.

Per-pixel depth metrics. We compute standard depth estimation metrics over valid pixels where ground truth depth is available. Depth error metrics include AbsRel (mean absolute relative error), RMSE (root mean squared error), and Log10 (mean absolute logarithmic error). Accuracy is measured using threshold metrics δ^1 , δ^2 , and δ^3 , which denote the percentage of pixels where the predicted-to-ground-truth depth ratio is below 1.25, 1.25^2 , and 1.25^3 , respectively. All metrics are computed with numerical safeguards, including epsilon clamping at 1e-6 to prevent division by zero and log-domain errors.

Occlusion boundary. We follow the evaluation protocol of the NYUv2-OC++ dataset (Ramamonjisoa et al., 2020) to assess occlusion boundary accuracy. Each predicted depth map is first min-max normalized, followed by the application of the OpenCV Canny edge detector (Canny, 1986) with low and high thresholds of 100 and 200 to produce a binary mask of predicted boundary pixels. Using the ground-truth boundary labels from NYUv2-OC++, we compute two metrics: ε_a (accuracy), the average distance from each predicted edge pixel to the nearest ground-truth edge; and ε_c (consistency), the average distance from each ground-truth edge pixel to the nearest predicted edge. Both are reported in squared pixels, where lower values indicate better alignment, and 0 denotes perfect correspondence.

3D scene reconstruction. We reconstruct 3D point clouds by back-projecting each pixel of the predicted depth maps into 3D space using the known camera intrinsics from the NYUv2 dataset, following the standard protocol for semantic scene completion (Song et al., 2017). To evaluate reconstruction quality, we compute the Chamfer distance between the predicted and ground truth point clouds. Recall quantifies how well the predicted points cover the ground truth surface, while precision measures how accurately the predicted points align with the true geometry.

Detailed evaluation protocol for **layout-aware retrieval** is provided in Section B, respectively.

B. Layout-aware Retrieval

Our architecture not only improves depth prediction but also facilitates structure-aware representation learning. First, SHED learns features that reflect scene layout, enabling more accurate layout-aware image retrieval than DPT (Ranftl et al., 2021). Second, its segment hierarchy captures geometric cues informed by depth supervision, whereas CAST (Ke et al., 2024) relies on visual cues.

We provide a detailed explanation of our proposed metric, *layout-aware retrieval*, which evaluates the structural quality of learned representations by measuring how well the model retrieves frames from the same 3D scene in a video, either across the full sequence or within nearby frames.

To compute this metric, we extract the [CLS] token from the final layer of the vision transformer in DPT and SHED for each image, denoted as $\mathbf{z}_{cls} \in \mathbb{R}^D$, and apply l_2 normalization. We then construct a full pairwise similarity matrix, where each entry is computed as the cosine similarity between l_2 -normalized image embeddings: $S_{ij} = \mathbf{z}_{cls}^{(i)} \cdot \mathbf{z}_{cls}^{(j)}$.



Figure 8. SHED learns layout-aware representations through depth supervision. We evaluate image retrieval on NYUv2 based on cosine similarity between class tokens from the final ViT block. **a)** Top-5 results (ranked left to right), with similarity scores shown below. SHED retrieves images with similar layouts, such as a central desk and a rear bookshelf, while DPT retrieves unrelated scenes. **b)** Top- K accuracy at the scene and frame level ($k = 5$), where the targets are different views from the same scene or nearby frames. SHED significantly outperforms DPT in all settings, indicating that our depth-guided segmentation effectively encodes spatial layout.

Retrieval performance is evaluated in two settings: *scene-level* and *frame-level*. In the scene-level setting, the goal is to retrieve other frames from the same annotated scene, testing the model’s ability to maintain structural consistency under varying viewpoints. In the frame-level setting, each frame is treated as an independent query, focusing on retrieving visually similar frames regardless of scene membership. We additionally define a frame- k variant, where retrieval is restricted to the k temporally adjacent frames, allowing us to assess the model’s sensitivity to local layout changes. We report top- K nearest neighbor retrieval accuracy on the NYUv2 (Nathan Silberman & Fergus, 2012) test set.

To further evaluate the robustness of layout-aware retrieval, we vary both the candidate set size (k) and the top- K threshold. A smaller k imposes a stricter constraint, requiring the model to identify the most similar frame from a limited pool. As shown in Figure 9, SHED consistently outperforms DPT across all settings. Performance improves for both methods as k increases, with the largest gap observed at low top- K values. These results suggest that SHED captures layout similarity more precisely and excels at retrieving the most relevant match.

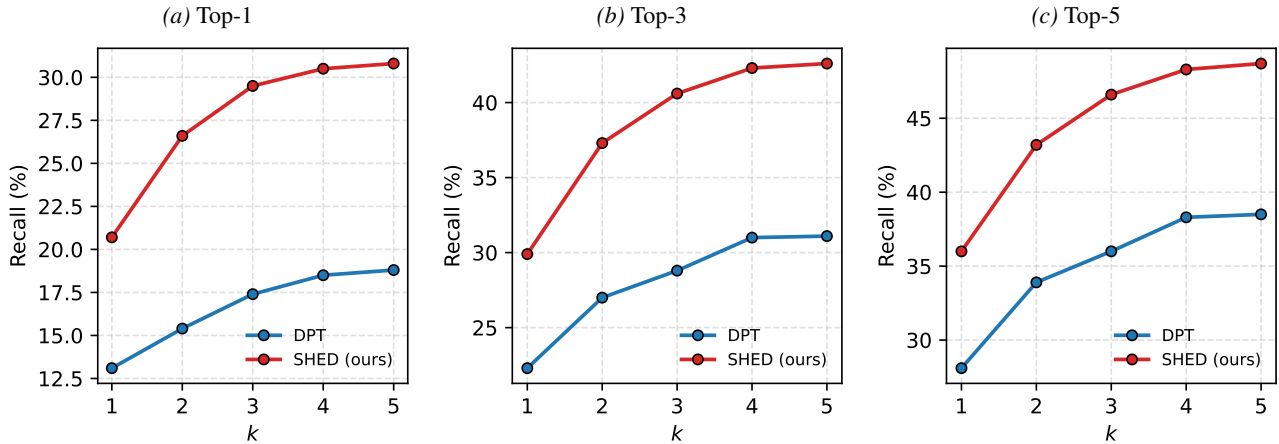


Figure 9. Frame- k recall with varying temporal range k . We report Top- K retrieval recall ($K \in \{1, 3, 5\}$) for DPT and SHED across temporal ranges $k \in [1, 5]$. The consistent gains highlight the robustness of our depth-supervised representation to spatial and viewpoint changes.

C. Evaluation on Diverse Benchmarks

we extend our experiments to a mixed-domain training setup using Virtual KITTI (Cabon et al., 2020), HyperSim (Roberts et al., 2021), and MegaDepth (Li & Snavely, 2018). We train the SHED using a uniform sampling strategy across all datasets for 20 epochs with batch size of 64. We then evaluate this model in a fully zero-shot manner on three unseen datasets, including KITTI (outdoor) (Geiger et al., 2013), NYUv2 (indoor) (Nathan Silberman & Fergus, 2012), SUN-RGBD (indoor) (Song et al., 2015).

Table 6. SHED improves mixed data setting. We evaluate standard depth accuracy and error metrics on more diverse dataset. SHED delivers competitive per-pixel depth estimation performance comparable to DPT when trained mixed training setting in cross-domain zero-shot evaluation.

Method	KITTI		NYUv2		SUN-RGBD	
	AbsRel \downarrow	$\delta > 1.25 \uparrow$	AbsRel \downarrow	$\delta > 1.25 \uparrow$	AbsRel \downarrow	$\delta > 1.25 \uparrow$
DPT	0.286	0.475	0.247	0.559	8.58	0.169
SHED (ours)	0.272	0.500	0.244	0.571	7.16	0.190

The results below demonstrate that SHED consistently outperforms the DPT baseline across domains, including both indoor and outdoor scenes. The segment-hierarchy inductive bias of SHED is not specific to the NYUv2 domain but transfers effectively to outdoor and mixed-domain settings, consistently outperforming the baseline.

D. Additional Visualizations

D.1. More visualizations of depth maps



Figure 10. Comparison of depth maps. SHED captures more accurate shapes with sharper boundaries, whereas DPT produces blurrier results.

D.2. More visualizations of image retrieval



Figure 11. Comparison of top-1 image retrieval results. SHED retrieves samples that are more structurally similar to the query, indicating that its global embedding effectively captures scene layouts. In contrast, DPT focuses more on visual appearance, as shown in column 3, where it retrieves an image from a different scene that shares a similar color of blue.

D.3. More visualizations of 3D reconstruction

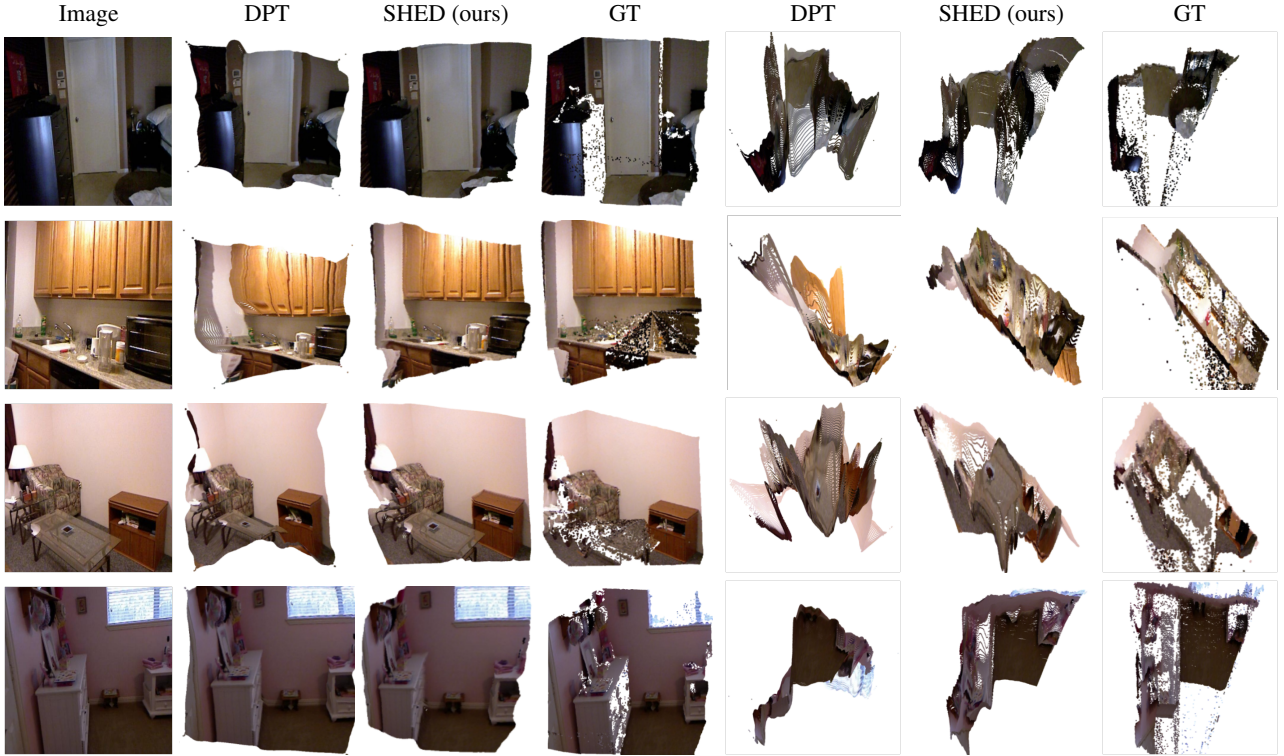


Figure 12. Comparison of 3D reconstruction results. Frontal views (cols 2–4) and bird’s-eye views (cols 5–7). DPT yields curved wall boundaries in the frontal views, which lead to distorted 3D reconstructions visible in the bird’s-eye views. In contrast, SHED produces sharp depth edges that preserve straight object contours and more faithfully represent the ground-truth 3D geometry.

E. Limitations and Broader Impacts

E.1. Limitations and future works

While SHED demonstrates strong structural coherence in depth estimation, its hierarchical design requires the number of tokens to be pooled at each level to be specified in advance. As a result, the unpooling process assumes a fixed correspondence between pooled and unpooled tokens, which may limit flexibility when the underlying scene structure does not align well with the predefined hierarchy. This design choice constrains the model to operate within a fixed hierarchical schedule, potentially reducing adaptability to scenes with highly varying structural complexity. A promising direction for future work is to relax this constraint by enabling adaptive or data-driven determination of the hierarchical schedule, allowing the model to adjust the number of tokens dynamically based on scene complexity. In addition, exploring more flexible unpooling mechanisms that do not require a strict one-to-one correspondence between pooled and unpooled tokens could further improve robustness to diverse scene layouts.

E.2. Broader impacts

Structured understanding of the 3D world and accurate depth estimation are central challenges in AI, with direct impact on safety-critical applications such as autonomous driving, augmented reality, and robotics. In practice, failures in these systems often result not from a lack of data but from insufficient structured reasoning, making predictions vulnerable to occlusion, unusual viewpoints, and dynamic environments. Our framework promotes geometry-aware perception by producing robust and interpretable depth estimates that align with scene structure. This can improve reliability in complex real-world settings and lead to systems with more transparent failure modes.